

# Variation of oxygen oxidation state at the base of Earth's lower mantle

E. Koemets<sup>1,\*</sup>, M. Bykov<sup>1,3</sup>, E. Bykova<sup>3</sup>, S. Chariton<sup>1</sup>, G. Aprilis<sup>4</sup>, S. Clément<sup>5</sup>, J. Rouquette<sup>5</sup>, J. Haines<sup>5</sup>, V. Cerantola<sup>6</sup>, K. Glazyrin<sup>3</sup>, A. Abakumov<sup>9</sup>, L. Ismailova<sup>9</sup>, C. McCammon<sup>1</sup>, V. B. Prakapenka<sup>11</sup>, M. Hanfland<sup>6</sup>, H.-P. Liermann<sup>3</sup>, I. Leonov<sup>7,8</sup>, A. V. Ponomareva<sup>8</sup>, I. A. Abrikosov<sup>10</sup>, N. Dubrovinskaia<sup>4</sup>, L. Dubrovinsky<sup>1</sup>

1. Bayerisches Geoinstitut, University of Bayreuth, D-95440 Bayreuth, Germany
3. Photon Science, Deutsches Elektronen-Synchrotron, D-22607 Hamburg, Germany
4. Material Physics and Technology at Extreme Conditions, Laboratory of Crystallography, Universität Bayreuth, D-95440 Bayreuth, Germany
5. Institut Charles Gerhardt Montpellier (UMR CNRS 5253), Université de Montpellier, F-34095 Montpellier cedex 5, France
6. ESRF-The European Synchrotron CS40220 38043 Grenoble Cedex 9 France
7. Institute of Metal Physics, Sofia Kovalevskaya Street 18, 620219 Yekaterinburg GSP-170, Russia
8. Materials Modeling and Development Laboratory, NUST "MISIS", 119049 Moscow, Russia
9. Skolkovo Institute of Science and Technology, Skolkovo Innovation Center, 143026 Moscow, Russia
10. Department of Physics, Chemistry and Biology (IFM), Linköping University, SE-581 83 Linköping, Sweden
11. Center for Advanced Radiation Sources, University of Chicago, Chicago, Illinois 60437, USA

\* Corresponding author

**Iron and oxygen interactions control oxygen fugacity and thus most of the global geochemical processes (1, 2). Extreme pressures and temperatures (PT) characteristic for Earth's deep interior are known to drastically affect the chemistry of these elements and to promote the formation of oxides unstable at ambient conditions, such as the homologous series of  $n\text{FeO}$   $m\text{Fe}_2\text{O}_3$  and  $\text{FeO}_2$  (3–6). To elucidate the chemistry of oxygen and the crystal chemistry of iron-oxygen compounds in detail, we use *in situ* single-crystal X-ray diffraction and Mössbauer spectroscopy in diamond anvil cells and 'density-functional theory plus dynamical mean-field theory' (DFT+DMFT) calculations. Here we report that at extreme PT conditions the oxidation state of oxygen in  $\text{FeO}_2$  is equal to 1.5-, and in major phases that constitute the lower mantle and the core-mantle boundary (CMB), the value deviates from 2-. The crystal chemistries of Fe,Al-bearing silicate perovskite (bridgmanite, Brg) and post-perovskite (PPv) considerably change: iron enters an octahedral structural position, the amount of iron in pure iron silicate perovskite and post-perovskite can be larger than the amount of silicon, and the quantity of iron in co-existing Brg and PPv may be significantly different. The formation of an oxygen reservoir in Earth's lower mantle (3, 7) is one of many consequences that can influence the dynamics and chemistry of the CMB, and alteration of the oxidation state of oxygen at high pressure as shown in this work can considerably contribute to this process.**

Iron is considered to be the only geochemically abundant element in Earth's interior with a variable oxidation state. At ambient or low pressures, three different iron oxides are known – Fe<sub>2</sub>O<sub>3</sub> (the mineral hematite), Fe<sub>3</sub>O<sub>4</sub> (magnetite, the oldest known magnetic material), and FeO (wüstite, typically non-stoichiometric and iron deficient). Recently numerous iron oxides with unexpected compositions (Fe<sub>4</sub>O<sub>5</sub>, Fe<sub>5</sub>O<sub>6</sub>, Fe<sub>7</sub>O<sub>9</sub>, Fe<sub>5</sub>O<sub>7</sub>, Fe<sub>25</sub>O<sub>32</sub> etc.), unusual crystal structures, and intriguing physical properties were synthesized at high pressures and high temperatures (HPHT) (5, 8–10). Hu et al. (11) reported a novel iron oxide FeO<sub>2</sub>. Its cubic symmetry and space group (*P* $\bar{a}$ 3) were established using multigrain analysis (6). The compound was interpreted as pyrite-structured ferrous iron peroxide, and the crystal structure was refined from powder X-ray diffraction (XRD) data on the basis of this model (6). The chemical nature of the FeO<sub>2</sub> compound still remains to be uncertain, ranging from a dioxide (with no direct chemical bonds between O<sup>2-</sup> oxygen ions) to a peroxide (with covalent bonds between oxygen atoms forming O<sub>2</sub><sup>2-</sup> anions) (12, 13). A straightforward way to elucidate the nature of the FeO<sub>2</sub> compound is to synthesize single crystals of FeO<sub>2</sub> and investigate them *in situ* in a diamond anvil cell (DAC).

Here we performed a series of synthesis experiments in DACs (see *Methods* in Supplementary Materials, Fig. S1, Table S1), obtained the single crystals, and applied synchrotron single-crystal X-ray diffraction and Mössbauer spectroscopy in order to clarify the structure of FeO<sub>2</sub> and the state of iron.

To perform the experiments, a foil of pure iron was placed in a DAC along with cryogenically loaded oxygen. Compression of iron in oxygen at ambient temperature to 25(1) GPa did not result in any chemical reaction. At this pressure, laser heating of the sample at ~1500(100) K led to formation of Fe<sub>2</sub>O<sub>3</sub> (space group R3-c, lattice parameters  $a = 6.271(7)$  Å,  $c = 7.662(4)$  Å) (Fig. S2), in agreement with literature data (8). After further pressure increase to 46(1) GPa the sample was laser heated at ~1200(100) K. The XRD pattern of the temperature quenched product appeared to be drastically different. XRD analysis led to the identification of a cubic FeO<sub>2</sub> phase with unit cell parameter  $a = 4.4313(14)$  Å, which is close to the values previously reported for “pyrite-type” FeO<sub>2</sub> (6, 13).

Iterative heating of the samples at different pressures led to the growth of single-crystal domains of the cubic FeO<sub>2</sub> phase, which were appropriate for obtaining XRD data of sufficient quality for structure solution and refinement (*Methods*, Tables S1, S2, S3). The structural

analysis showed that the shortest O-O distance varies from 2.203(4) Å to 2.090(10) Å within the pressure range ~36 to ~73 GPa. From the crystal-chemical point of view, such a large value for the shortest O-O distance suggests the absence of chemical bonding between these oxygen atoms. Thus, the cubic FeO<sub>2</sub> structure (Fig. 1) belongs to the HP-PdF<sub>2</sub> structure type (14, 15) (see also Supplementary Discussion), rather than to the pyrite-type.

An explicit examination of the calculated electronic structure (see Methods, Fig. S13 and Fig. S14) and charge density distribution (Fig. 1) confirms that the oxidation state of Fe in HP-PdF<sub>2</sub>-type FeO<sub>2</sub> is close to 3+ and that there is a noticeable absence of O-O bonding to at least 180 GPa. Mössbauer spectroscopy data (Fig. S4) are consistent with iron in the Fe<sup>3+</sup> state (3, 16). Our experimental and theoretical results (Fig. 1 and *Supplementary Information*) thus imply that the oxidation state of oxygen in HP-PdF<sub>2</sub>-type FeO<sub>2</sub> is equal to 1.5- due to oxygen-metal negative charge transfer (Fig. S13). Such a charge transfer is expected to shorten the Fe-O distance and consequently the volume of FeO<sub>6</sub> octahedra, which should lead to both iron polyhedra and the entire structure becoming very incompressible. Indeed, fitting the pressure-volume data for cubic FeO<sub>2</sub> with the Birch-Murnaghan equation of state (EoS) gave EoS parameters with a large bulk modulus:  $V_0=97.6(3)$  Å<sup>3</sup>/unit cell, bulk modulus  $K_0=305(9)$  GPa, and  $K'=4.0$  (fixed). Compressibility of FeO<sub>6</sub> octahedra is very low ( $K_{0,\text{octahedron}}=350(4)$  GPa) and their volume is significantly smaller than that known for any other compound, including those with ferric iron Fe<sup>3+</sup> in the low-spin state (Fig. 2).

Our results show that HP-PdF<sub>2</sub>-type iron dioxide FeO<sub>2</sub> can form at ~45 GPa. Although this pressure corresponds to a depth of ~1150 km within the upper part of Earth's lower mantle, the appearance of FeO<sub>2</sub> in this deep region is hardly possible, since the high oxidation state of iron Fe<sup>3+</sup> is not plausible for any equilibrium homogeneous lower-mantle assemblage with oxygen fugacity below the iron-wüstite buffer (2). However, prominent changes in oxygen chemistry could affect the behavior of major lower mantle phases, particularly those containing iron (such as bridgmanite, Brg), and the effect should be most pronounced for iron-rich compounds.

Formation of pure Fe-bridgmanite with composition Fe<sub>0.88</sub>SiO<sub>3</sub> (generalized perovskite formula ABO<sub>3</sub>, A=Fe<sup>2+</sup><sub>0.64</sub>Fe<sup>3+</sup><sub>0.24</sub>, B=Si) was reported (17) to be a result of a transformation of skiaegite-majorite garnet Fe<sub>1.19</sub>Si<sub>0.81</sub>O<sub>3</sub> at high temperatures and pressures of 45 to 110 GPa. Heating this garnet to ~2500(150) K above 125 GPa resulted in the formation of a mixture of

perovskite- and post-perovskite-structured phases, and of pure post-perovskite above ~145 (see *Supplementary Materials*). In Fe-bridgmanite synthesized below 110 GPa the iron content is lower than the silicon content and iron is absent in the B-site. However the refinement of single-crystal XRD data for Fe-bridgmanite at 141(3) GPa, for example, resulted in the composition  $\text{Fe}_{0.92(2)}(\text{Si}_{0.85(4)}\text{Fe}_{0.15(4)})\text{O}_3$ , and  $\text{Fe}_{0.92(4)}(\text{Si}_{0.88(2)}\text{Fe}_{0.12(4)})\text{O}_3$  for post-perovskite at 144(3) GPa (Table S4; according to XRD, oxygen positions are fully occupied). This means that (a) iron enters octahedrally coordinated B-sites, (b) within measurement uncertainty the transformation from skiaegite-majorite garnet to high-pressure phases is isochemical, and (c) pure iron silicate post-perovskite really exists (Fig. 3)

Such drastic changes in crystal-chemistry suggest that chemical bonding in silicate phases at conditions of the lower part of the lower mantle should also change. Indeed, for both perovskite and post-perovskite  $\text{Fe}(\text{Si}_{0.75}\text{Fe}_{0.25})\text{O}_3$  phases in which the B-site is 25% occupied by iron atoms, DFT+DMFT simulations (see *Methods and Supplementary Discussion*) with unit cell volume corresponding to ~140 GPa predict that  $\text{Fe}^{2+}$  and  $\text{Fe}^{3+}$  will be located in the A and B sites, respectively, and that the oxygen oxidation state (which is equal to 2- in  $\text{FeSiO}_3$ ) will remarkably change and become ~ 1.9- due to formation of a hole on oxygen sites. The alteration of the oxidation state of oxygen is similar to that found for  $\text{FeO}_2$ , although mechanisms of the change are different for the silicate and oxide systems (see *Methods*, Fig. S15).

Single-crystal XRD supported by Mössbauer spectroscopy (see *Methods and Supplementary Discussion*) allow the determination of the amount of ferric iron in Fe-bridgmanite or post-perovskite. For example, for Fe-bridgmanite synthesized at 100 GPa the resulting composition is  $\text{Fe}^{2+}_{0.71}\text{Fe}^{3+}_{0.17}\text{SiO}_3$ . The total cation charge is thus equal to 5.93+, which within uncertainty implies an oxygen oxidation state equal to 2-. In the case of Fe,Al-bearing post-perovskite synthesized at 155 GPa, the analysis (Fig. S11) gives the formula  $\text{Mg}_{0.86}\text{Fe}^{2+}_{0.12}\text{Fe}^{3+}_{0.02}\text{Si}_{0.91}\text{Al}_{0.04}\text{O}_3$  and a total cation charge of 5.78+, thus the formal charge on oxygen is less than 2- in accordance with theoretical predictions.

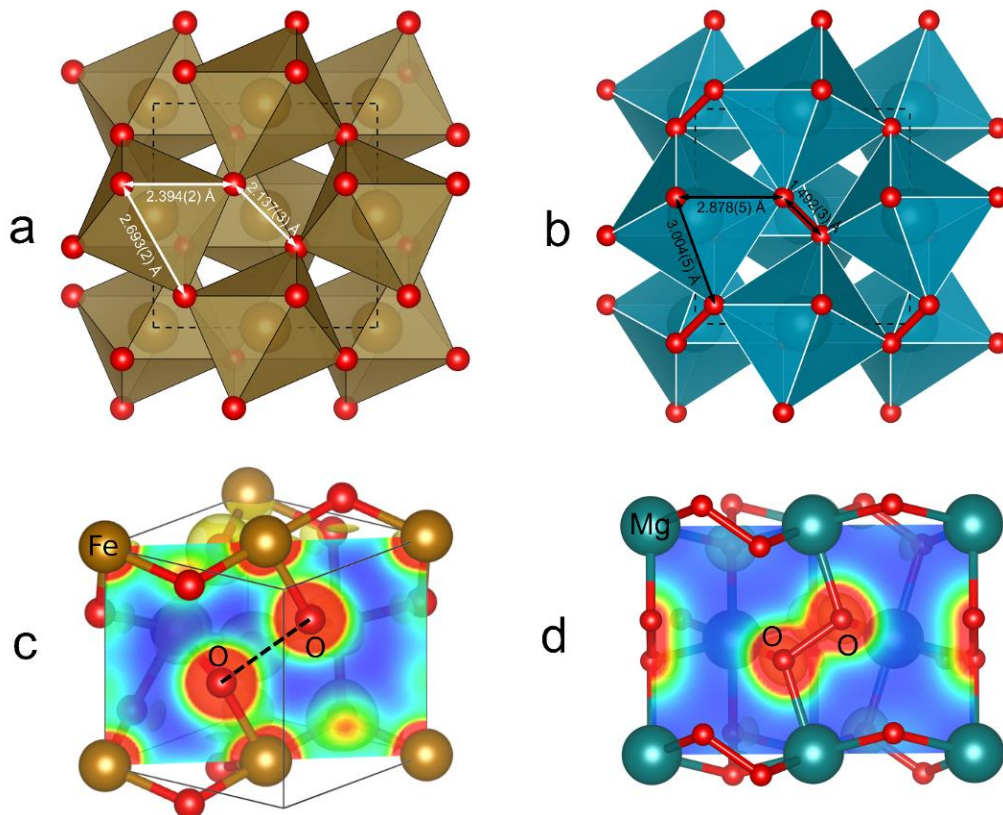
Laser heating of a single crystal of silicate perovskite  $\text{Mg}_{0.60}\text{Fe}_{0.40}\text{Si}_{0.63}\text{Al}_{0.37}\text{O}_3$  (see FE37 in Table S4 and *Supplementary Materials*) at 153(5) GPa and 2700(150) K resulted in the formation of several single-crystal domains with the lattice parameters of bridgmanite and post-perovskite (Table S4). Post-perovskite domains (for example,  $(\text{Mg}_{0.77},\text{Fe}_{0.23})(\text{Si}_{0.62},\text{Al}_{0.37})\text{O}_3$ ,

Table S4) show an almost two-times iron depletion in comparison with the initial bridgmanite. In contrast, crystallites with the perovskite structure are enriched with iron (for example,  $(\text{Mg}_{0.42}, \text{Fe}_{0.68})(\text{Si}_{0.57}, \text{Al}_{0.37}, \text{Fe}_{0.06})\text{O}_3$ , Table S4) and accommodate a small amount of iron at the B-site. Silicate perovskites with such a large iron content are not stable at low (or ambient) pressure (18, 19) and should decompose. Indeed, TEM analysis (*Supplementary Materials*) of a sample recovered to ambient conditions reveals its chemical inhomogeneity, including the appearance of submicron-size crystals of magnetite ( $\text{Fe}_3\text{O}_4$ ). The observation of magnetite ( $\text{Fe}^{2+}/\Sigma\text{Fe}=0.33$ ) is remarkable, because iron in the starting perovskite was nearly pure ferric iron ( $\text{Fe}^{2+}/\Sigma\text{Fe}=0.07(3)$  (20), and the presence of  $\text{Fe}_3\text{O}_4$  supports the inference that the course of transformation at  $\sim 150$  GPa leads to ferric iron being partially reduced by oxygen.

Experiments on single crystals of Fe,Al-bearing bridgmanite with different compositions  $(\text{Mg}_{1-x}, \text{Fe}_x)(\text{Si}_{1-y}, \text{Al}_y)\text{O}_3$  ( $x=0.12-0.17$ ;  $y=0.03-0.06$ ) (particularly the samples designated as FE17 and FE14 in (17) and Table S4, see *Supplementary Materials*) were performed at pressures of 137 to 155 GPa and temperatures of 2400 – 2700 K. In all cases, the formation of only silicate perovskite and post-perovskite phases was observed, but due to the small overall iron concentration and the relatively large uncertainties associated with harsh experimental conditions, it is difficult to draw quantitative conclusions regarding the chemical composition of the products of reactions and the oxidation state of iron. Still, formation of domains of phases with slightly different unit cell parameters/volumes was observed in all experiments (Table S4), and, as a rule, the amount of iron in post-perovskite is smaller than in co-existing (or starting) perovskite. In some cases there is evidence that iron is incorporated in the B-site: for example, upon heating of sample FE17 at 142(3) GPa, a perovskite domain with a composition  $(\text{Mg}_{0.82(4)}, \text{Fe}_{0.18(4)})(\text{Si}_{0.92(5)}, \text{Fe}_{0.08(5)})\text{O}_3$  formed (Table S4).

The substantially reduced oxidation state of oxygen confirmed in HP-PdF<sub>2</sub>-type FeO<sub>2</sub> and evident in silicate PPv suggests that at certain high-pressure high-temperature conditions, i.e. starting from a certain depth in the Earth's interior (Fig. 4), a larger amount of oxygen is required in order to balance the same amount of cations compared to lower PT conditions. This could contribute to the formation of an oxygen reservoir in the Earth's lower mantle (3, 7), which can influence the dynamics and chemistry of the core-mantle boundary (CMB). Our *in situ* single-crystal diffraction data show that at pressures relevant for the D'' layer at the CMB, silicate post-

perovskite is depleted in iron with respect to initial (or co-existing) Fe,Al-bearing bridgmanite. This agrees with reports of a drastic increase in iron partitioning into ferropericlase compared to silicate in the stability field of post-perovskite (21, 22), probably associated with changes in the oxidation states of iron and oxygen (22, 23). Variations in the oxidation state of iron and partitioning of differently oxidized species between co-existing phases can be one reason for the large transformation pressure range across the bridgmanite-post-perovskite boundary (24). A significant difference in densities of co-existing bridgmanites and post-perovskites (for example, in FE17 (Table S4), the densities of co-existing silicate perovskite and post-perovskite are  $6.00(3) \text{ g/cm}^3$  and  $5.84(3) \text{ g/cm}^3$ , respectively) may lead to dynamic instabilities at the bottom of the lower mantle, formation of rising plumes and accumulation of dense material forming global-scale heterogeneities such as large low-shear-velocity provinces (LLSVPs) detected by seismic observations (25), nearly antipodal beneath the Pacific Ocean and Africa. Evidence for chemical differences between these regions and the surrounding mantle includes sharp margins and anti-correlated anomalies between bulk and shear sound velocities in LLSVPs. Although the identity and origin of these regions is still unknown, the likely high density of LLSVPs may be explained by enrichment in iron (26) and linked to the changes in oxygen chemical behavior.



**Fig. 1. Comparison of crystal structures of HP-PdF<sub>2</sub>-type FeO<sub>2</sub> and pyrite-type MgO<sub>2</sub> peroxide.** (a) Crystal structure of cubic (HP-PdF<sub>2</sub>-type) FeO<sub>2</sub> as refined from single-crystal XRD data (iron – brown, oxygen – red). XRD data were taken from the temperature quenched sample obtained after heating iron in oxygen at 58(1) GPa and 1800(100) K in a DAC (Tables S1, S2). The shortest experimentally determined O-O distance is 2.137(2) Å, which is too large for a peroxide-type structure and prevents consideration as a pyrite-type. (b) Crystal structure of pyrite-type MgO<sub>2</sub> peroxide (magnesium atoms – blue-green) at ambient conditions (27). The shortest O-O distance is 1.492(3) Å. (c) Valence electron density plot for cubic FeO<sub>2</sub> for the unit cell volume 83.0 Å<sup>3</sup> (corresponding to ~69 GPa). We performed a full structural optimization and computed the lattice parameters and the electronic properties of the HP-PdF<sub>2</sub>-type crystal structure of FeO<sub>2</sub>, using a fully charge self-consistent DFT+DMFT approach (*Methods*, Fig. S12, S13). The theory confirms that the shortest O-O bond length even at a pressure as high as 180 GPa remains sufficiently large (~1.86 Å), suggesting the *absence* of covalent ‘molecular’ (O<sub>2</sub>)<sup>3-</sup> bonding in FeO<sub>2</sub>. (d) Valence electron density plot for cubic MgO<sub>2</sub> for the unit cell volume 113.3 Å<sup>3</sup> (ambient pressure) as obtained by DFT (HSE03) calculations. For MgO<sub>2</sub> the formation of ‘molecular’ (O<sub>2</sub>)<sup>2-</sup> bonds, with ~21% of a maximal electron density value in the center of the O-O contact, is evident. In contrast, for cubic FeO<sub>2</sub> the maximal electron density at the center of the shortest O-O contact is only ~5% and thus the calculations support the Fe<sup>3+</sup>(O<sup>1.5-</sup>)<sub>2</sub> electronic configuration. As non-integral values, the oxygen oxidation states seem to contradict the recently given refined generic definition of oxidation state as ‘the atom’s charge after ionic approximation of its heteronuclear bonds’ (28). The solution to overcome the limitation of the ionic approximation is found in modern computational chemistry allowing a proper accounting of electron distribution around atoms (29) and calculation of oxidation states from first principles (30). In the case of FeO<sup>1.5-</sup><sub>2</sub>, the value of 1.5- (O<sup>1.5-</sup>), which is considerably different from 2- (O<sup>2-</sup>) which is common for oxides, thus describes the partial atomic charge that accounts for the average number of electrons assigned to oxygen atoms in HP-PdF<sub>2</sub>-type FeO<sub>2</sub> and can be explained by an oxygen-metal negative charge transfer (Fig. S14).

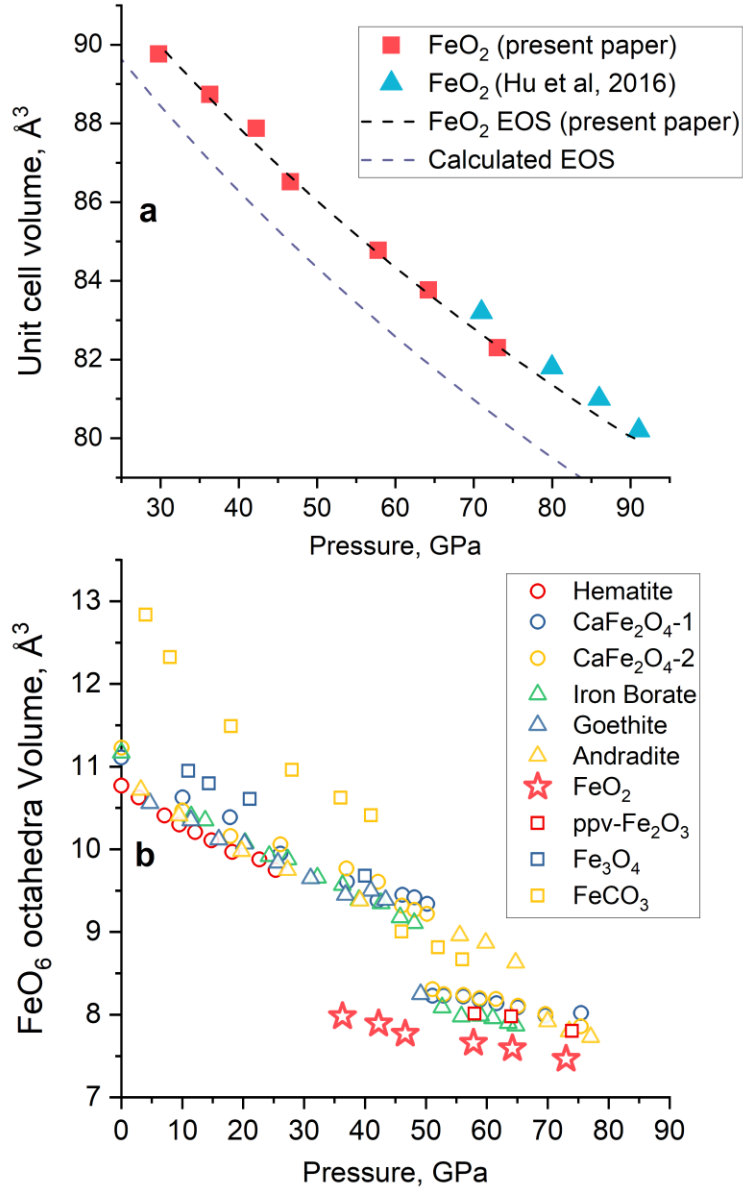


**Fig. 2. Compressional behaviour of HP-PdF<sub>2</sub>-structured cubic FeO<sub>2</sub>.** (a) Variation of the unit cell volume as a function of pressure: red squares – single-crystal XRD data, dashed black line – fit of this P-V data with the Birch-Murnaghan equation of state ( $V_0=97.6(3) \text{ \AA}^3$ ,  $K_0=305(9) \text{ GPa}$ ,  $K'=4.0$  (fixed)); blue triangles – powder XRD data according to Hu et al. (6). The EoS parameters obtained on the basis of our experimental data are close to those theoretically calculated by the DFT+DMFT method ( $V_0=99.6 \text{ \AA}^3$ ,  $K_0=270 \text{ GPa}$ ,  $K'=4.0$ ) which are in agreement with earlier simulations (31). (b) Pressure dependence of volumes of FeO<sub>6</sub> octahedra in various compounds according to (30) and references therein. Red open stars designate the data for HP-PdF<sub>2</sub>-structured cubic FeO<sub>2</sub>; red circles – hematite ( $\alpha$ -Fe<sub>2</sub>O<sub>3</sub>); blue and yellow circles – two different octahedra in calcium ferrite (CaFe<sub>2</sub>O<sub>4</sub>-1) and (CaFe<sub>2</sub>O<sub>4</sub>-2), respectively; green triangles – iron borate (FeBO<sub>3</sub>); blue triangles – goethite ( $\alpha$ -FeOOH); yellow triangles – andradite (Ca<sub>3</sub>Fe<sub>2</sub>(SiO<sub>4</sub>)<sub>3</sub>); open red squares – CaIrO<sub>3</sub>-type structured  $\eta$ -Fe<sub>2</sub>O<sub>3</sub> (ppv-Fe<sub>2</sub>O<sub>3</sub>); blue squares – magnetite (Fe<sub>3</sub>O<sub>4</sub>); yellow squares – iron carbonate (FeCO<sub>3</sub>).



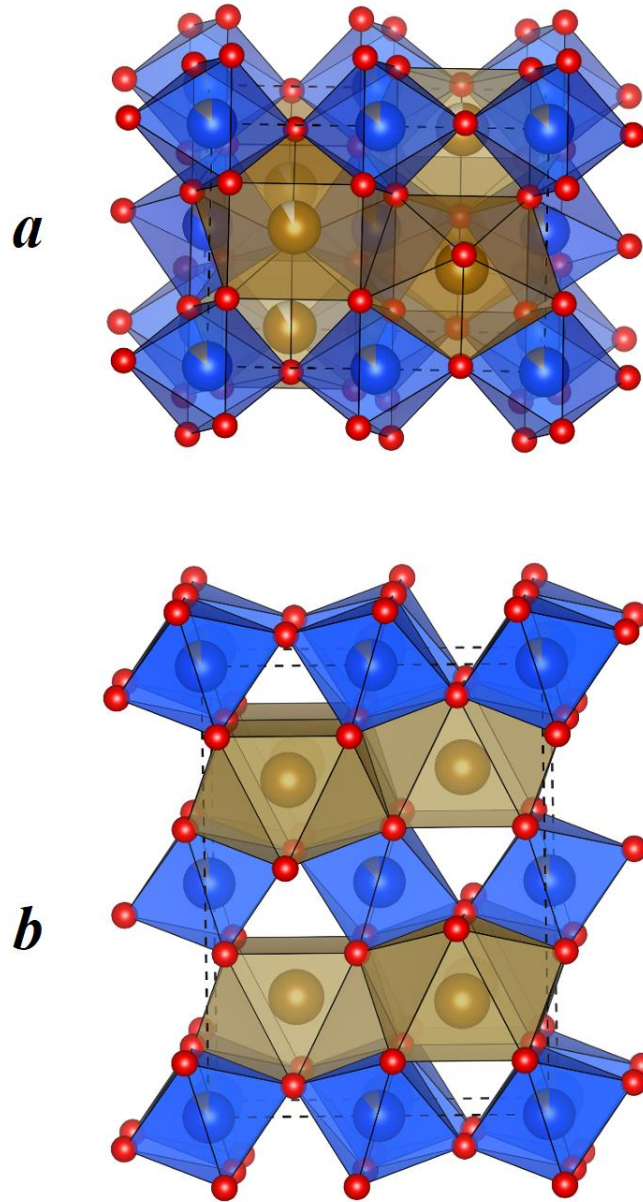


**Fig. 3. Experimentally determined crystal structures of pure-iron  $\text{CaIrO}_3$ -structured silicate post-perovskite and  $\text{GaFeO}_3$ -structured orthorhombic silicate perovskite bridgmanite. (a)** Iron post-perovskite synthesized at 144(3) GPa and 2700(150) K with chemical composition  $\text{Fe}_{0.92(4)}(\text{Si}_{0.88(2)}\text{Fe}_{0.12(4)})\text{O}_3$ . **(b)** Fe-bridgmanite synthesized at 143(3) GPa and 2500(150) K with chemical composition  $\text{Fe}_{0.92(2)}(\text{Si}_{0.85(4)}\text{Fe}_{0.15(4)})\text{O}_3$  (see also Tables S1, S4). Crystal structures of both materials are built up from bi-capped prisms ("A-site", light brown) and octahedra ("B-site", blue) formed by oxygen atoms (red spheres). In Fe-bridgmanite octahedra are linked through vertices forming a 3D network, and in post-perovskite edge-sharing octahedra are arranged in columns that are combined through vertices to form 2D layers. Fe cations are shown as brown spheres, and Si as blue spheres. According to single-crystal XRD data, iron cations enter B-sites (Si-positions) of the structures (this is designated by brown segments in the blue spheres).

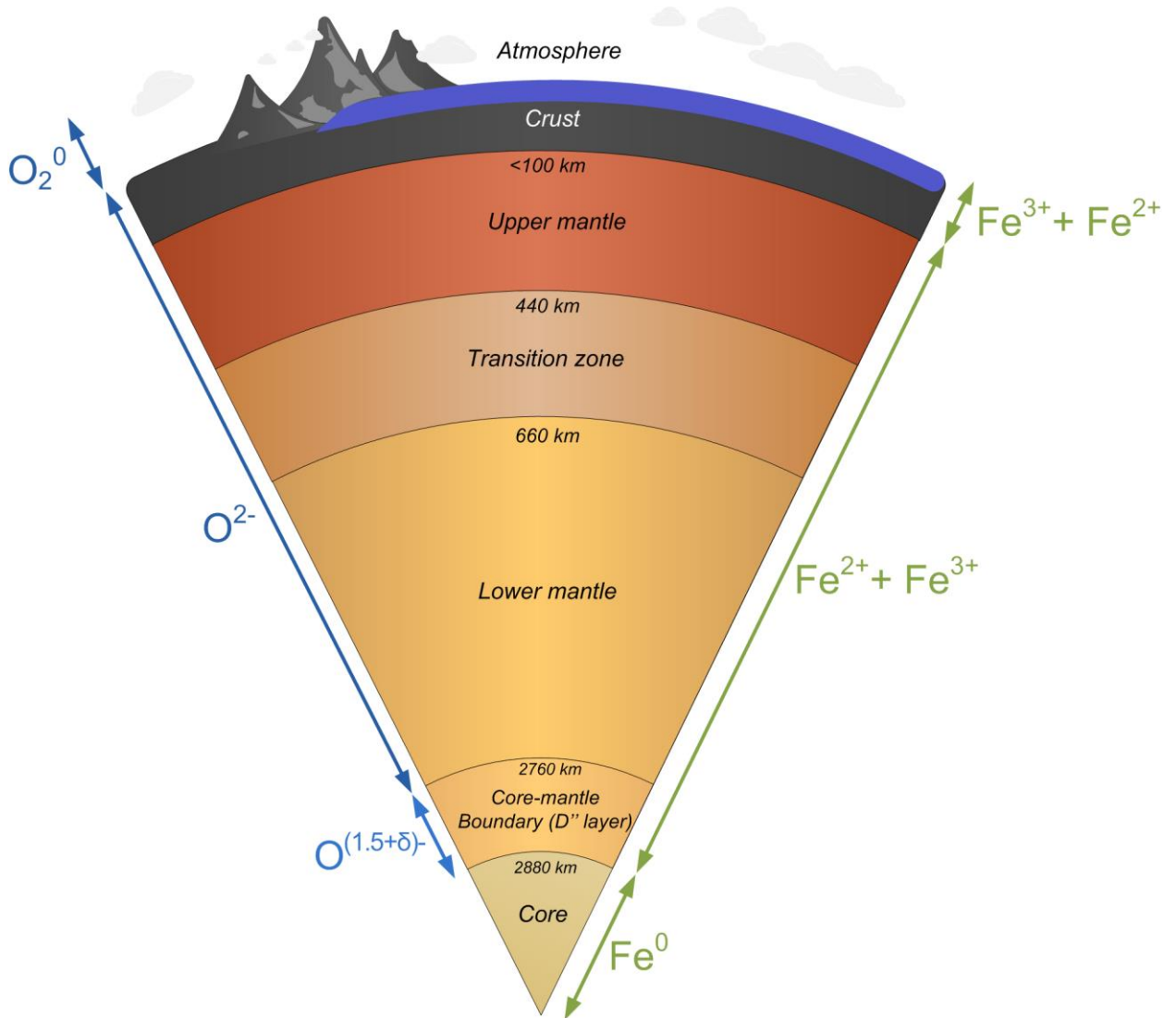


**Fig. 4. Schematic diagram showing variation of iron and oxygen oxidation states through different geospheres.** Iron and oxygen interactions control oxygen fugacity and thus most of global geochemical processes (1, 2). So far, iron has been considered to be the only geochemically abundant element within the solid Earth to have a variable oxidation state. In the crust and the upper mantle, the amount of ferric iron is higher than in the lower mantle (2) while the Earth's core is formed of iron alloys. Our experiments and earlier data (6) demonstrate that at pressures up to ~45 GPa, the most oxygen-rich oxide is  $\text{Fe}_2\text{O}_3$ . At higher pressures HP-PdF<sub>2</sub>-structured cubic  $\text{FeO}_2$  with  $\text{O}^{1.5-}$  becomes stable. While the crust and mantle are dominated by  $\text{O}^{2-}$ , near the core-mantle boundary the oxidation state of oxygen changes and may be described as  $\text{O}^{(1.5+\delta)-}$  ( $\delta < 0.5$ ;  $\delta \sim 0.43$  in silicate post-perovskite). For clarity the thickness of Earth layers is not drawn to scale.

## References

1. C. Ballhaus, R. F. Berry, D. H. Green, Oxygen fugacity controls in the Earth's upper mantle. *Nature*. **348**, 437 (1990).
2. D. J. Frost, C. A. McCammon, The Redox State of Earth's Mantle. *Annu. Rev. Earth Planet. Sci.* **36**, 389–420 (2008).
3. E. Bykova *et al.*, Structural complexity of simple Fe<sub>2</sub>O<sub>3</sub> at high pressures and temperatures. *Nat. Commun.* **7**, 10661 (2016).
4. R. Sinmyo *et al.*, Discovery of Fe<sub>7</sub>O<sub>9</sub>: a new iron oxide with a complex monoclinic structure. *Nat. Publ. Gr.*, 1–7 (2016).
5. B. Lavina, Y. Meng, Unraveling the complexity of iron oxides at high pressure and temperature: Synthesis of Fe<sub>5</sub>O<sub>6</sub>. *Sci. Adv.* **1**, e1400260–e1400260 (2015).
6. Q. Hu *et al.*, FeO<sub>2</sub> and FeOOH under deep lower-mantle conditions and Earth's oxygen–hydrogen cycles. *Nature*. **534**, 241–244 (2016).
7. D. Andrault *et al.*, Large oxygen excess in the primitive mantle could be the source of the Great Oxygenation Event, 5–10 (2018).
8. E. Ito *et al.*, Determination of high-pressure Phase equilibria of Fe<sub>2</sub>O<sub>3</sub> using the Kawai-type apparatus equipped with sintered diamond anvils. *Am. Mineral.* **94**, 205–209 (2009).
9. A. B. Woodland, J. Kornprobst, A. Tabit, Ferric iron in orogenic lherzolite massifs and controls of oxygen fugacity in the upper mantle. *Lithos.* **89**, 222–241 (2006).
10. B. Lavina *et al.*, Discovery of the recoverable high-pressure iron oxide Fe<sub>4</sub>O<sub>5</sub>. **108** (2011), doi:10.1073/pnas.1107573108.
11. Q. Hu *et al.*, Dehydrogenation of goethite in Earth's deep lower mantle. *Proc. Natl. Acad. Sci.* **114**, 201620644 (2017).
12. S. S. Streltsov, A. O. Shorikov, S. L. Skornyakov, A. I. Poteryaev, D. I. Khomskii, Unexpected 3+ valence of iron in FeO<sub>2</sub>, a geologically important material lying “in between” oxides and peroxides. *Sci. Rep.* **7**, 1–6 (2017).
13. A. T. Garcia-Sosa, M. Castro, Density functional study of FeO<sub>2</sub>, FeO<sub>2</sub><sup>+</sup>, and FeO<sub>2</sub><sup>-</sup>. *Int. J. Quantum Chem.* **80**, 307–319 (2000).
14. J. Haines *et al.*, Structural characterisation of the pa $\bar{3}$ -type, high pressure phase of ruthenium dioxide. *J. Phys. Chem. Solids.* **59**, 239–243 (1998).
15. Y. Shirako *et al.*, Synthesis, Crystal Structure, and Electronic Properties of High-Pressure PdF<sub>2</sub>-Type Oxides MO<sub>2</sub> (M = Ru, Rh, Os, Ir, Pt). *Inorg. Chem.* **2**, 11616–11625 (2014).
16. P. Gütllich, E. Bill, A. X. Trautwein, *Mössbauer spectroscopy and transition metal chemistry: fundamentals and applications* (Springer Science & Business Media, 2010).

17. L. Ismailova *et al.*, Stability of Fe , Al-bearing bridgmanite in the lower mantle and synthesis of pure Fe-bridgmanite. *Sci. Adv.* **2**, 1–8 (2016).
18. H. K. Mao, G. Shen, R. J. Hemley, Multivariable dependence of Fe-Mg partitioning in the lower mantle. *Science (80-. )*. **278**, 2098–2100 (1997).
19. S. M. Dorfman, Y. Meng, V. B. Prakapenka, T. S. Duffy, Effects of Fe-enrichment on the equation of state and stability of (Mg,Fe)SiO<sub>3</sub> perovskite. *Earth Planet. Sci. Lett.* **361**, 249–257 (2013).
20. K. Glazyrin *et al.*, Magnesium silicate perovskite and effect of iron oxidation state on its bulk sound velocity at the conditions of the lower mantle. *Earth Planet. Sci. Lett.* **393**, 182–186 (2014).
21. R. Sinmyo, K. Hirose, Iron partitioning in pyrolitic lower mantle. *Phys. Chem. Miner.* **40**, 107–113 (2013).
22. H. Piet *et al.*, Spin and valence dependence of iron partitioning in Earth’s deep mantle. *Proc. Natl. Acad. Sci.* **113**, 11127–11130 (2016).
23. C. Prescher, F. Langenhorst, L. S. Dubrovinsky, V. B. Prakapenka, N. Miyajima, The effect of Fe spin crossovers on its partitioning behavior and oxidation state in a pyrolitic Earth’s lower mantle system. *Earth Planet. Sci. Lett.* **399**, 86–91 (2014).
24. K. Catalli, S. H. Shim, V. Prakapenka, Thickness and Clapeyron slope of the post-perovskite boundary. *Nature*. **462**, 782–785 (2009).
25. A. M. Dziewonski, V. Lekic, B. A. Romanowicz, Mantle Anchor Structure: An argument for bottom up tectonics. *Earth Planet. Sci. Lett.* **299**, 69–79 (2010).
26. J. Trampert, Probabilistic Tomography Maps Chemical Heterogeneities Throughout the Lower Mantle Probabilistic Tomography Maps Chemical Heterogeneities Throughout the Lower Mantle. **853** (2014), doi:10.1126/science.1101996.
27. A. Kjekshus, T. Rakke, Preparations and properties of magnesium, copper, zinc, and cadmium dichalcogenides. *Acta Chem. Scand. Ser. A.* **33**, 617–620 (1979).
28. P. Karen, P. McArdle, J. Takats, Comprehensive definition of oxidation state (IUPAC Recommendations 2016). *Pure Appl. Chem.* **88**, 831–839 (2016).
29. A. Walsh, A. A. Sokol, J. Buckeridge, D. O. Scanlon, C. R. A. Catlow, Oxidation states and ionicity. *Nat. Mater.*, 1 (2018).
30. V. Postils, C. Delgado-Alonso, J. M. Luis, P. Salvador, An Objective Alternative to IUPAC’s Approach To Assign Oxidation States. *Angew. Chemie - Int. Ed.* **57**, 10525–10529 (2018).
31. A. O. Shorikov, S. V. Streltsov, Equation of state of FeO 2. *J. Magn. Magn. Mater.* (2017), doi:10.1016/j.jmmm.2017.10.061.
32. D. M. Vasiukov *et al.*, Pressure-induced spin pairing transition of Fe<sup>3+</sup> in oxygen octahedra, 1–41 (2017).

## Acknowledgments

Portions of this work were performed at GeoSoilEnviroCARS (The University of Chicago, Sector 13), Advanced Photon Source (APS), Argonne National Laboratory. GeoSoilEnviroCARS is supported by the National Science Foundation - Earth Sciences (EAR - 1634415) and Department of Energy- GeoSciences (DE-FG02-94ER14466). This research used resources of the Advanced Photon Source, a U.S. Department of Energy (DOE) Office of Science User Facility operated for the DOE Office of Science by Argonne National Laboratory under Contract No. DE-AC02-06CH11357.

Support provided by the Swedish Research Council project No. 2015-04391, the Swedish Government Strategic Research Areas in Materials Science on Functional Materials at Linköping University (Faculty Grant SFO-Mat-LiU No. 2009-00971) and the Swedish e-Science Research Centre (SeRC) is gratefully acknowledged.

Theoretical analysis of chemical bonding was supported by the Russian Science Foundation (Project No. 18-12-00492). Simulations of the electronic structure were supported by the Ministry of Education and Science of the Russian Federation in the framework of Increase Competitiveness Program of NUST "MISIS" (Project No. K3-2018-001) implemented by a governmental decree dated March 16th 2013, No. 211.

## Author contributions

E.K., N.D., L.D. designed and planned experiments.

E.K., S.Cl. and J.R. performed cryogenic loading of a sample.

E.K., M.B., E.B., S.C., G.A., S.Cl., J.R., J.H., K.G., L.I., V.P., M.H., H.-P.L. and L.D. conducted the HPHT single-crystal X-ray diffraction experiments.

E.K., M.B., E.B. and L.D. analysed the data from HPHT single-crystal XRD experiments.

The SMS spectra were collected by E.K., G.A., S.C., V.C., C.M. and C.M. together with L.D. interpreted the results.

A.A. performed TEM measurements.

I.L., A.P., I.A. performed DFT+DMFT calculations and interpreted the results.

E.K., C.M., N.D. and L.D. wrote the manuscript with contributions of all authors.

**Competing financial interests:** The authors declare no competing financial interests.